

**Airborne Spectral Measurements of Surface-Atmosphere
Anisotropy During the SCAR-A, Kuwait Oil Fire, and
TARFOX Experiments**

PETER F. SOULEN^{1,2}, MICHAEL D. KING², SI-CHEE TSAY²,
G. THOMAS ARNOLD³, AND JASON Y. LI³

Short title: BRF Measurements from SCAR-A, KOFSE, and TARFOX

Journal of Geophysical Research - Atmospheres

Manuscript submitted March 18, 1999

Manuscript revised September 2, 1999

¹ Joint Center for Earth Systems Technology: University of Maryland Baltimore County.

² NASA Goddard Space Flight Center, Greenbelt, Maryland.

³ SM&A Corporation(East), 901 Follin Lane, Suite 400, Vienna, Virginia.

Authors – Dr. Peter F. Soulen

NASA Goddard Space Flight Center

Code 913

Greenbelt, MD 20771

soulen@climate.gsfc.nasa.gov (Internet)

Dr. Michael D. King — Corresponding author

NASA Goddard Space Flight Center

Code 900

Greenbelt, MD 20771

(301) 614-5636

king@climate.gsfc.nasa.gov (Internet)

(301) 614-5620 (fax)

Dr. Si-Chee Tsay

NASA Goddard Space Flight Center

Code 913

Greenbelt, MD 20771

(301) 614-6188

Mr. G. Thomas Arnold

SM&A Corporation (East)

901 Follin Lane, Suite 400

Vienna, VA 22180

(301) 614-6229

Mr. Jason Y. Li
SM&A Corporation (East)
901 Follin Lane, Suite 400
Vienna, VA 22180
(301) 614-6230

ABSTRACT

During the SCAR-A, Kuwait Oil Fire Smoke Experiment, and TARFOX deployments, angular distributions of spectral reflectance for various surfaces were measured using the scanning Cloud Absorption Radiometer (CAR) mounted on the nose of the University of Washington C-131A research aircraft. The CAR contains 13 narrowband spectral channels between 0.47 and 2.3 μm with a 190° scan aperture (5° before zenith to 5° past nadir) and 1° instantaneous field of view. The bidirectional reflectance is obtained by flying a clockwise circular orbit above the surface, resulting in a ground track approximately 3 km in diameter within about two minutes.

Spectral bidirectional reflectances of four surfaces are presented: the Great Dismal Swamp in Virginia with overlying haze layer, the Saudi Arabian Desert and Persian Gulf in the Middle East, and the Atlantic Ocean measured east of Richmond, Virginia. Although the CAR measurements are contaminated by atmospheric effects, results show distinct spectral characteristics for various types of surface-atmosphere systems, including hot spots, limb brightening and darkening, and sunglint. In addition, the hemispherical albedo of each surface-atmosphere system is calculated directly by integrating over all high angular-resolution CAR measurements for each spectral channel. Comparing the nadir reflectance with the overall hemispherical albedo of each surface, we find that using nadir reflectances as a surrogate for hemispherical albedo can cause albedos to be underestimated by as much as 95% and overestimated by up to 160%, depending on the type of surface and solar zenith angle.

1. INTRODUCTION

To better understand how the Earth's climate and ecosystems function, we need a greatly improved understanding of what affects the Earth's radiation budget, and how it varies both spatially and temporally. One of the major goals of the Earth Observing System (EOS) is to use satellite instruments to measure the top-of-the-atmosphere angular distribution of the radiance field on a global scale, and to determine from these measurements parameters that are essential to understanding the Earth's climate, such as cloud and aerosol optical thickness [King and Greenstone, 1999]. Because satellite-measured radiances are affected by both the atmosphere and the underlying surface, it is not possible to properly interpret these measurements unless we obtain a more detailed understanding of how different surfaces on the Earth reflect solar radiation. To assist in this effort, the Cloud Absorption Radiometer (CAR) [King *et al.*, 1986], a multispectral scanning radiometer developed at Goddard Space Flight Center, has been flown aboard the University of Washington Convair C-131A aircraft many times over the last decade to measure the bidirectional reflectances (BRFs) of several types of natural surfaces.

CAR BRF data have now been processed for several different surfaces. King [1992] presented BRF measurements of smoke from the Kuwait oil fires during the Kuwait Oil Fire Smoke Experiment (hereafter referred to as KOFSE). Tsay *et al.* [1998] presented BRFs of cerrado, dense forest, and a thick smoke layer over dense forest measured in Brazil during the Smoke, Clouds, and Radiation - Brazil (SCAR-B) experiment. Arnold *et al.* [1999] presented BRFs of tundra and sea ice measured in the Arctic during the Arctic Leads Experiment (LEADEx) and the Arctic Radiation Measurements in Column Atmosphere-surface System (ARMCAS) experiment. Additional examples of BRF data from sea ice and Arc-

tic stratus clouds can be found in *Curry et al.* [1999]. In this work, we present recently processed BRF measurements of four other surfaces: a forested wetland with an overlying haze layer, Saudi Arabian desert with overlying desert dust, Persian gulf water with some overlying aerosol, and Atlantic ocean with sun glint, measured during three field campaigns: the Sulfates, Clouds, and Radiation – Atlantic (SCAR-A) experiment, KOFSE, and the Tropospheric Aerosol Radiative Forcing Observational Experiment (TARFOX). To our knowledge, only the airborne POLDER instrument is capable of gathering similar multispectral BRF data with comparable high angular resolution (small instantaneous field of view, or IFOV) and sampling from as many viewing angles within a short period of time [*Bréon et al.*, 1997].

For general circulation models or global climate models (GCMs), it is important to use good estimates of the surface hemispheric albedo [*Barnsley et al.*, 1994]. This parameter is often estimated by assuming that the underlying surface is Lambertian (isotropic), and using the nadir-reflectance as measured from an airborne or satellite instrument as a surrogate. In this work, we compare the measured nadir-reflectance of each surface with the hemispherical surface-atmosphere albedo, calculated from the high angular-resolution CAR measurements, to quantify the bias that can occur when this approximation is used [e.g., *Kimes et al.*, 1987].

Plots of the BRF in the principal plane suggests that the BRFs could be parameterized simply with a few independent variables, which would be useful for modeling studies [*Ahmad and Deering*, 1997]. Such parameterization, together with atmospheric correction of the data for Rayleigh scattering, gaseous absorption, and aerosol effects, will be reported in future work.

The following section lists the definition of surface bidirectional reflectance

function (BRF) used in this work, and briefly includes some considerations in applying it to remote sensing applications. The instrumentation and data collection strategy are presented in Section 3, followed by a discussion of each field experiment, measured spectral anisotropy of each surface-atmosphere system, and albedo calculations in Section 4. A brief summary of this study and an overview of future work is given in Section 5.

2. DEFINITIONS AND CONSIDERATIONS

Although there is more than one definition of the spectral bidirectional reflectance distribution function, we use the definition of bidirectional reflection function (BRF, R_λ) found in *van de Hulst* [1980], given as

$$R_\lambda(\theta, \theta_0, \phi) = \frac{\pi I_\lambda(\theta, \theta_0, \phi)}{\mu_0 F_\lambda}, \quad (1)$$

where θ and θ_0 are the viewing and illumination zenith angles, respectively; ϕ is the azimuthal angle between the viewing and illumination directions; $\mu_0 = \cos \theta_0$; I_λ is the corresponding reflected radiance; and F_λ is the collimated irradiance. The collimated irradiance F_λ is computed by weighting the solar flux at the top of the atmosphere with the spectral response function of each band, taking into account the effects of the elliptical orbit of the earth around the sun.

To use Eq. (1) to define surface BRF, we implicitly make two assumptions: (1) that the reflectances we measure are not significantly affected by the atmosphere, and (2) that reflectance does not change with position above the surface, or that the surface is homogeneous. To address the first assumption, all of the CAR channels were carefully selected to minimize effects of gaseous absorption. Sensitivity studies indicate that Rayleigh scattering and gaseous absorption should reduce atmospheric transmittance in any of the channels by 3-12% at most, and future atmospheric correction of these BRF data should be straight-

forward [cf. *Tsay et al.*, 1998 for a more detailed discussion]. To address the second assumption, we chose our target surface areas to ensure that the underlying surface was as homogeneous as possible (e.g., to make sure that there were no ponds of water in the middle of the targeted forested wetland area).

The spectral albedo r_λ for each surface is calculated by integrating over the BRF, which is approximated by summing up radiances received by the detector from all viewing directions/solid angles (IFOVs). Using this approximation, r_λ becomes

$$\begin{aligned} r_\lambda(\theta_0) &= \frac{1}{\pi} \int_0^{2\pi} \int_0^{\pi/2} R_\lambda(\theta, \theta_0, \phi) \cos\theta \sin\theta \, d\theta \, d\phi, \\ &\cong \frac{1}{\mu_0 F_\lambda} \left[\sum_{i=1}^M \sum_{j=1}^N I_\lambda(\theta_i, \theta_0, \phi_j) \cos\theta_i \sin\theta_i \Delta\theta_i \Delta\phi_j \right], \end{aligned} \quad (2)$$

where (i, j) are respectively the indices of (θ, ϕ) for discretization (M, N terms) over the hemisphere. Because the spectral BRF measurements by the CAR have very fine angular resolution (i.e., $M = 90$ samples in θ and $N \approx 200$ in ϕ , cf. Table 1), approximating the integral as a sum over the radiance measurements obtained at discrete angles does not produce significant computational error. By using Eq. (2), it is straightforward to compute the spectral hemispherical albedo for each CAR-measured surface, which can then be compared with its average measured nadir reflectance.

3. INSTRUMENTATION AND DATA COLLECTION

During SCAR-A, KOFSE, and TARFOX, surface bidirectional reflectances of various surfaces were measured using the Cloud Absorption Radiometer (CAR), a multispectral scanning radiometer that was designed and built initially for the purpose of measuring the angular distribution of scattered radiation deep within a cloud layer [cf. *King et al.*, 1986 for details]. The CAR was mounted in the nose

of the University of Washington C-131A research aircraft during each of these experiments. The CAR scans in a vertical plane on the right hand side of the aircraft from 5° before zenith to 5° past nadir (190° aperture) with an IFOV of 1° , thereby permitting observations of both the zenith and nadir radiances to be obtained with as much as a 5° aircraft roll, an angle that is measured simultaneously with a gyroscope aboard the aircraft. Table 1 summarizes the specifications of the CAR.

The optical system of the CAR is non-dispersive, being composed of a complex configuration of dichroic beam splitters and narrowband interference filters. The CAR provides radiometric measurements at 13 discrete wavelengths: 0.472 (or 0.503), 0.675, 0.754, 0.869, 1.038, 1.219, 1.271, 1.552, 1.643, 1.725, 2.099, 2.207, and 2.303 μm . In general, the bandwidth of the CAR channels is ~ 20 nm, except for the filter wheel channels where $\Delta\lambda \approx 40$ nm. The first 7 channels of the radiometer were continuously and simultaneously sampled, while the eighth was selected from among the 6 channels on the filter wheel (ranging from 1.552-2.303 μm). While the filter wheel is usually set to rotate to measure a new wavelength interval after a preset number of scans, the filter wheel can also be locked at a particular channel. Because the magnitude of the measured radiance can vary widely, the CAR provides for 7 manual gain settings that apply a uniform gain adjustment to all eight electrical channels simultaneously. This manual gain setting, which permits greater flexibility in field operations, is output to the data system for retrieval.

To measure the BRF of a surface, the plane banks at a comfortable roll angle of $\sim 20^\circ$ and flies in a circle about 3 km in diameter above the surface (see Figure 1) for roughly two minutes. At an altitude of 600 m above the targeted surface area and 1° IFOV, the pixel resolution is about 10 m at nadir and about 270 m at

an 80° viewing angle from the CAR. Replicated observations (multiple circular orbits) were acquired over most selected surfaces so that average BRFs could be produced that averaged out small-scale surface inhomogeneities.

We believe using the CAR in this approach is the most mobile and efficient way of measuring surface BRFs. A more detailed comparison between using the CAR and other methods to gather surface BRFs may be found in *Tsay et al.*, [1998].

4. RESULTS FROM OBSERVATIONS

To reconstruct a bidirectional reflectance distribution from CAR measurements, we assume that the surface area is homogeneous. This requires us to choose our target surface areas to be as homogeneous as possible. In this work, we present spectral BRFs for four types of surface-atmosphere systems measured during SCAR-A, KOFSE, and TARFOX: (1) forested wetland with haze layer, measured over the Great Dismal Swamp south of Norfolk, Virginia at approximately 36.5°N , 76.5°W under clear-sky conditions from 13:13 to 13:22 UTC on July 28, 1993; (2) desert, acquired in Saudi Arabia at approximately 27.6°N , 48.5°E under clear-sky conditions, from 12:28 to 12:30 UTC on May 28, 1991; (3) gulf water, acquired in the Persian Gulf at approximately 28.4°N , 50.0°E , with clear-sky above, from 13:03 to 13:07 UTC on May 28, 1991; and (4) ocean water, acquired east of Richmond, Virginia at approximately 37.8°N , 72.6°W , under clear-sky conditions, from 16:34 to 16:43 UTC on July 27, 1996. Plate 1 shows a Landsat thematic mapper image of the Saudi Arabian desert acquired in 1990, one year before the Kuwaiti oil fires, as well as a photograph of the Great Dismal Swamp taken from the University of Washington C-131A aircraft during SCAR-A.

Below, we will document and discuss the results of BRF measurements obtained from the CAR for these four types of surfaces. In addition, we will compare the hemispherical albedo calculated using Eq. (2) with the measured nadir-reflectance of each surface-atmosphere system. It must be noted that uncertainties in estimates of calculated hemispherical albedo and measured nadir-reflectance do not include possible errors due to instrument calibration.

4.1 *Forested Wetland with a Haze Layer on July 28, 1993*

In July 1993, the SCAR-A field experiment was conducted around the western Atlantic Ocean. Two of the main scientific objectives of SCAR-A were (1) to measure surface reflectance in the spectral range 0.44-3.9 μm for different types of surfaces from several view directions to better characterize their bidirectional reflectance properties, and (2) to measure the apparent spectral reflectance including aerosol scattering of different types of surfaces from several view directions to test algorithms for remote sensing of aerosols and atmospheric correction for satellite sensors. Two research aircraft were deployed: the NASA ER-2, and the University of Washington C-131A. The MODIS Airborne Simulator (MAS) [King *et al.*, 1996], a scanning multispectral imager, was flown aboard the ER-2, while the CAR was flown aboard the C-131A. During a two week period, both aircraft took off from their base at Wallops Flight Facility on Wallops Island, Virginia, and flew over several regions, including Hog Island, the Great Dismal Swamp in southern Virginia, the Pine Barrens in New Jersey, Atlantic City, and over parts of the Atlantic Ocean.

On July 28, both the ER-2 and the C-131A flew over the Great Dismal Swamp at different times. Plate 2 shows a false-color composite image of the Great Dismal Swamp, acquired by the MAS as the ER-2 flew from top to bottom down the center of this image at an altitude of ~ 21 km. The false-color image was con-

structed by contrast stretching and combining three separate channels into one 24-bit image, where the spectral channels were assigned to red, green, and blue (RGB) 8-bit display channels. For this scene, the RGB assignment was 2.14 μm (red), 0.94 μm (green), and 0.66 μm (blue). In this manner the vegetation appears green, clear-cut forest magenta, lakes, rivers, and open water dark blue, urban development purple, and sun glint white. The bright yellow line to the left of Lake Drummond represents the “hot spot” or “opposition surge” [Hapke, 1993], which was observed continuously as the NASA ER-2 aircraft flew over the region at a heading of 208° with the MAS scan at a relative azimuth of 187° . In addition, sunglint in the specular direction is evident over surface water on the right-hand side of the image. This image was acquired when the solar zenith angle θ_0 was $\sim 31^\circ$, and has been resampled to a constant 60 m resolution.

To measure the BRF of the Great Dismal Swamp, the C-131A made four circular orbits. The filter wheel channel was locked on the 2.21 μm channel for the first two orbits, and was then locked on the 1.64 μm channel for just more than one orbit. During this observational period (~ 9 min), the solar zenith angle varied by only 2° (from 53.17° to 54.84° ; cf. Table 2). Although the sky was free of clouds, the Great Dismal Swamp was covered by a haze layer. According to sunphotometers from nearby ground stations [Holben *et al.*, 1998], the aerosol over the area had an Ångström exponent of 1.41 ± 0.03 with an optical thickness of about 0.4 at 0.441 μm , which is considerably less than usual [SCAR-A Mission Summary Report, 1994].

Plate 3 illustrates the spectral BRF measured over the Great Dismal Swamp on this day. In all polar plots, the viewing zenith angle is represented as the radial distance from the center, and azimuth as the length of arc on the respective zenith circle. The principal plane (i.e., the vertical plane containing the sun) re-

sides in the 0° - 180° azimuthal plane with the sun located in the 180° azimuthal direction. With this definition, the upper half circle represents forward scattering and the lower half represents backscattering, with the anti-solar direction at $\theta_0 \approx 54^{\circ}$ shown as a white spot in Plate 3a. These BRFs have been averaged over all four orbits, except for those of the two filter-wheel channels, one of which was averaged over two orbits ($1.64 \mu\text{m}$) while only one full orbit of data was obtained for the other filter wheel channel ($2.21 \mu\text{m}$). While averaging the BRFs over all orbits has further smoothed and symmetrized the data, the BRFs from individual circles are not very different from one another.

In Plate 3, there are two striking features: (1) a highly symmetric pattern about the principal plane, and (2) a strong reflection in the backscattering direction ($\phi = 180^{\circ}$) peaked at a zenith angle of $\sim 60^{\circ}$. The high degree of symmetry indicates that the surface and atmosphere were quite homogeneous, while the observed strong backscattering signal at wavelengths from 0.75 - $1.64 \mu\text{m}$ is the hot spot coinciding with the anti-solar direction (n.b., the hot spot is also discernable at $2.21 \mu\text{m}$). For this BRF, aside from the hot spot and the forward scattering horizon, the reflection functions have values ranging from 0.25 to 0.6 at wavelengths between $0.87 \mu\text{m}$ and $1.27 \mu\text{m}$. Spectral and angular information, such as the amplitude and width of the hot spot feature, may be linked with specific biophysical parameters, such as biomass density [e.g., *Strahler and Jupp*, 1990] and canopy geometry [*Jupp and Strahler*, 1991]. In the visible (0.47 - $0.68 \mu\text{m}$), the surface spectral anisotropy that is observed in other channels is diminished, as is the magnitude of the reflectance, although there is significant limb brightening. Previous work shows that BRFs of forests should be most anisotropic at visible wavelengths because chlorophyll absorption causes strong shadowing, with shadow-hiding causing strong hot spot effects that are maximized in the visible

[*Hapke et al.*, 1996; *Deering et al.*, 1999]. However in Plate 3, the BRF in the visible appears to be more isotropic, probably due to Rayleigh scattering and aerosol effects. The considerable limb brightening in the forward direction is consistent with a more absorbing surface exhibiting low orders of scattering [*Chandrasekhar*, 1960].

Plate 4 shows the detailed angular distribution of bidirectional reflectance in the principal plane at various wavelengths. A principal plane plot of forested wetland reflectance (Plate 4a) using MAS data presented in Plate 2 shows that the hot spot, located at around 31° in the backscattering direction, is very distinct. Another principal plane plot of forested wetland reflectance (Plate 4b) using CAR data gathered earlier in the day shows that the hot spot is less distinct when the solar zenith angle is larger (54°), although it still has strong spectral dependence. The shape of the hot spot varies; it is most pronounced in the 0.87-1.27 μm range, and becomes smaller in magnitude and broader in shape towards longer wavelengths, while it is suppressed altogether at visible wavelengths due in large part to atmospheric effects. These BRF characteristics may be related to the multiple scattering among leaves with particular leaf angle distributions [e.g., *Ross and Marshak*, 1989], along with Leaf Area Index, canopy vertical geometry (heights of trees and understory layers), reflectance of the underlying surface (wetland with occasional standing water), spectral properties of all canopy elements, and shadowing caused by trunks, branches, and leaves [*Deering et al.*, 1999]. Reflection functions for all channels show limb brightening in the forward scattering direction near the horizon, and to a lesser extent limb darkening in the backscattering direction for all non-visible wavelengths. Although this surface-atmosphere system is one of the most complex, the polar plot and the principal plane plot of this system suggest that its large-scale bidirectional reflectance

could be modeled fairly simply; the functions are more or less smooth. Future modeling should determine how the large-scale BRF of forested wetland with overlying haze aerosol can be parameterized.

The spectral hemispherical albedo of this surface-atmosphere system is also of interest. Table 2 lists the central wavelength and bandwidths of each CAR channel, together with its corresponding solar flux. The solar flux was calculated at the central wavelength for each CAR spectral response function using MODTRAN [Berk *et al.*, 1989]. For each channel, Table 2 also lists the variation of solar zenith angle during the period of data collection as well as the hemispherical albedo calculated using Eq. (2). It must be noted that no estimates of uncertainty were made for the surface-atmosphere hemispheric albedo at 2.21 μm because we do not have any repeated measurements (i.e., only one orbit was completed). Since the solar zenith angle changes by less than 2° over the 9-minute period required to obtain these measurements, uncertainties in the albedos are much more likely due to surface inhomogeneity than changes in surface illumination. Also in Table 2, the nadir reflectances are presented. The measured nadir reflectance is typically 15-20% less than the computed hemispherical albedo at most wavelengths, except in the visible channels (0.47 and 0.68 μm), where the measured nadir reflectances are about 60% less than the computed albedos due in part to the much stronger atmospheric effects in the visible compared to the near-infrared (see Table 2a). Using measured nadir reflectance as a surrogate for hemispherical albedo may result in significantly underestimating surface-atmosphere albedo for a larger solar zenith angle ($\sim 54^\circ$). This may be seen most clearly in Plate 5, which presents the hemispherical albedo, nadir reflectance, and their ratio for each surface-atmosphere system reported in Table 2. It must be pointed out that, while estimates of hemispherical albedo (Plate 5a) and nadir

reflectance (Plate 5b) depend on the accuracy of instrument calibration, the ratio of the nadir reflectance to hemispherical albedo (Plate 5c) does not depend on calibration.

Later in the day, the C-131A measured the BRF of the Great Dismal Swamp in the same area as just described. The four orbits took only 9 minutes, during which the smaller solar zenith angle ($\sim 20^\circ$) varied by only 1° . Again, only two orbits of BRF data were obtained at $1.64\ \mu\text{m}$, while only one orbit of BRF data was obtained at $2.21\ \mu\text{m}$; hence we make no estimate of uncertainty for hemispherical surface-atmosphere albedo at $2.21\ \mu\text{m}$. The later BRF is qualitatively quite similar to the BRF presented here, except there is less limb brightening. In this case, the measured nadir-reflectance was 7-14% more than the calculated surface albedo at most wavelengths, except for the visible channels, where the measured nadir reflectances were 30-40% less than the hemispherical albedos due in part to the much stronger atmospheric effects in the visible compared to the near-infrared (see Table 2b and Plate 5).

4.2 *Saudi Arabian Desert with Haze Layer on May 28, 1991*

In February 1991, the Iraqi army set 611 oil wells, storage tanks, and refineries ablaze as they fled Kuwait. The resulting fires produced large plumes of smoke that had significant effects on the Persian Gulf region but limited global effects. Between May 16 and June 12, 1991, the Kuwait Oil Fire Smoke Experiment (KOFSE) was conducted in the Persian Gulf Region [Hobbs and Radke, 1992]. During this time, some 550 oil wells were still burning in Kuwait. The purpose of KOFSE was to determine the chemical and physical nature of the smoke and to investigate its potential effects on air quality, weather, and climate. During this experiment, BRFs of various surfaces were measured as well.

The University of Washington C-131A aircraft flew over Kuwait, Saudi Ara-

bia, and the Persian Gulf during this experiment. On May 28, 1991, the CAR made one circular orbit over the desert of Saudi Arabia. During this orbit, the filter wheel was never set to any one channel; the filter wheel rotated throughout the orbit. As a result, the CAR did not sample enough reflectances to comprise a full BRF measurement for any of the 6 filter wheel channels. However, the other 7 channels made continuous measurements throughout the orbit. During this orbit, the solar zenith angle changed by less than 0.5° within a time period of just over 2 minutes. Records from this flight indicate that the surface was very dry, the sky was entirely free of clouds, but also that the desert surface was covered in haze that appeared to be desert dust instead of smoke. Incidents of smoke were observed to correlate strongly with increased concentrations of carbon dioxide (~ 100 ppm). Because the concentration of carbon dioxide was not at an elevated level around the time that this desert BRF distribution was measured (figure not shown), we conclude that the aerosol in the atmosphere is most likely desert dust rather than oil fire smoke. Because there were no sunphotometers on the ground near the BRF site, it is not known precisely what the aerosol optical thickness below the aircraft was on this day. However, a Total-Direct-Diffuse multichannel Radiometer (TDDR) flown on the C-131A aircraft estimated the overlying aerosol above the aircraft (altitude: 3.5 km) to have an Ångström exponent of 0.8 ± 0.2 and an optical thickness of 0.12 at $0.500 \mu\text{m}$ [Pilewskie and Valero, 1992].

Plate 6 shows the spectral BRF of the desert obtained on this day. Because only one orbit was obtained, it was not possible to average over multiple BRFs to smooth the data. In contrast to the BRF measured over the Great Dismal Swamp, this BRF is quite asymmetric, suggesting that the underlying surface-atmosphere system was somewhat inhomogeneous, which could be explained by inhomogeneity in the surface, aerosol layer, or both. For example, perhaps the surface con-

sisted of preferentially oriented sand dunes, as observed in a flat dune by *Deering et al.* [1990].

Considering the location of the anti-solar point located near 48.2° (marked by a white dot in Plate 6a), there appears to be a suggestion of a diffuse hot spot in Plate 6f. However, upon examination of the principal plane plot in Plate 4c, there does not appear to be any significant hot spot. In the principal plane, the reflection function is very smooth, with some limb brightening in the forward scattering direction for all channels. Desert surfaces such as flat dunes are often characterized by predominant forward scattering, and our measured BRF distribution seems to roughly match that of the flat dune measured by *Deering et al.* [1990]. However, the dune-flat BRF of *Deering et al.* [1990] had more backscattering. It is possible that effects of desert dust may be suppressing the surface anisotropy. Caution must be used in interpreting the data at $0.503\ \mu\text{m}$; notes made just before and after KOFSE indicate there may be errors in the absolute calibration of the $0.503\ \mu\text{m}$ channel.

Calculated surface-atmosphere system albedos for this desert surface are in Table 2c and Plate 5a. Because we do not have repeated BRF measurements at any wavelength (i.e., only one orbit was completed), we do not make any estimate of the uncertainty of error in our hemispherical surface-atmosphere system albedos. For this desert surface, the measured nadir-reflectances were 7-13% less than the hemispherical albedo, except for the $0.503\ \mu\text{m}$ channel, where the nadir-reflectance is 24% less than the calculated albedo (see Plate 5c) due in part to the much stronger atmospheric effects in the visible compared to the near infrared.

4.3 Persian Gulf on May 28, 1991

On the same flight that the desert BRF was measured, about half an hour later, the University of Washington C-131A aircraft flew over the Persian Gulf. This time, the CAR made two orbits over the Gulf. Again, the filter wheel was set to rotate frequently throughout the orbit, so that no full BRF could be constructed from CAR radiance measurements for any of the 6 filter wheel channels. During these two orbits, the solar zenith angle changed by only 1° within a time period of 4 minutes. As before in the desert case, records from this flight indicate that the sky was entirely free of clouds, and that there was less haze over the Persian Gulf than over the Saudi Arabian Desert. Although the visual records do not indicate a dark smoke layer, the somewhat increased concentration of carbon dioxide around the period when the Gulf water BRF distribution was measured indicates that there may have been some smoke aerosol present in the atmosphere. However, the data record of carbon dioxide concentration is extremely erratic during this time, which indicates that the estimates of carbon dioxide concentration may be in error. Although it is not known precisely what the aerosol optical thickness was over the Gulf on this day, the TDDR indicates that the aerosol above the aircraft (altitude: 2.3 km) had an optical thickness of 0.033 at $0.500 \mu\text{m}$ [Pilewskie and Valero, 1992]. However, the data indicate that the TDDR's performance was sporadic during this part of the flight (only 1 or at most 2 of the channels were functioning at all during this time), so this estimate of optical thickness may not be accurate, and there are not enough data to estimate the Ångström exponent.

Plate 7 shows the spectral BRF of the Persian Gulf that was obtained on this day. The BRF for the Gulf is very symmetric, indicating spatially homogeneous conditions, and very smooth. In general, the bidirectional reflectance function is

less than 0.1, except for the striking brightening in the forward scattering direction. This is not merely limb brightening, which does not vary significantly as a function of azimuthal angle; this is sunglint. Usually, sunglint occurs at the same viewing polar angle as the solar zenith angle, but in this case the sunglint angle appears to be about 10° greater than the incident solar angle. We believe this is due to atmospheric effects. When grazing emergence due to atmospheric effects superimposes onto the signal due to sunglint, the resulting signal appears to be a sunglint angle that is greater than the incident solar angle. There also appears to be some slight limb brightening in the backscattering direction, again due to atmospheric effects.

The principal plane plot of Persian Gulf reflectance in Plate 8a makes clear that sunglint and limb brightening in the backscattering direction have strong spectral dependence. (The flattening of the BRF between $60\text{-}90^\circ$ in the forward scattering direction for $1.22\ \mu\text{m}$ indicates that this channel was saturated.) In the principal plane, the reflection function is very smooth. There is some limb brightening in the forward scattering direction for all channels. Again, we note that records indicate there may have been errors in the absolute calibration of the $0.503\ \mu\text{m}$ channel.

Calculated surface-atmosphere system albedos for the Persian Gulf are presented in Table 2d and Plate 5a. In this case, the measured nadir-reflectance was 55% less than the hemispherical albedo for the $0.503\ \mu\text{m}$ channel, and it was 66-74% less than the hemispherical albedo for all other channels due mainly to the large influence of the sunglint at this solar zenith angle.

4.4 *Atlantic Ocean on July 27, 1996*

In July 1996, TARFOX was conducted to gather data on the direct effects of tropospheric aerosols on regional radiation budgets in cloud-free skies, while si-

multaneously measuring the chemical, physical, and optical properties of the aerosols. Data obtained during this experiment were also used to validate aerosol optical thickness retrievals. As in SCAR-A, the primary aircraft base for TARFOX was the NASA Wallops Flight Facility at Wallops Island, Virginia.

On July 27, 1996, the CAR was used to measure bidirectional reflectances of the Atlantic Ocean approximately 340 km offshore of Richmond, Virginia. During these measurements, the sky was free of clouds. Also mounted on the aircraft with the CAR, the six-channel NASA Ames Airborne Tracking Sunphotometer (AATS-6) measured optical thicknesses of aerosols above the altitude of the aircraft. During the recording of this BRF distribution, the AATS-6 recorded an aerosol layer (altitude: 0.28 km) with an Ångström exponent of 1.8 ± 0.1 with an optical thickness of 0.180 ± 0.003 at $0.451 \mu\text{m}$. The C-131A aircraft made four orbits over the ocean, with the filter wheel channel locked on 1.643 and $2.207 \mu\text{m}$ for two loops each. During these four orbits, the solar zenith angle changed by less than 0.5° within a time period of 9 minutes.

Plate 9 shows the spectral BRF of ocean water that was obtained on this day. The spectral range of the BRF for the Atlantic Ocean is very small, with sunglint opposite to the anti-solar point (indicated by a white dot in Plate 9a). The BRF appears highly symmetric, indicating spatially homogeneous conditions, and is very smooth. In general, the reflectance function is less than 0.1, with very slight limb brightening in both the forward scattering and backscattering directions, although limb brightening is more pronounced for shorter wavelengths ($0.472\text{--}0.675 \mu\text{m}$) due to scattering by aerosols in the atmosphere.

The principal plane plot of the Atlantic Ocean reflectance (Plate 8b) makes clear that, in this case, sunglint does not have strong spectral dependence. We have analyzed several measured BRF distributions of ocean water, and we con-

clude that sunglint has weak spectral dependence when the solar zenith angle is small, and strong spectral dependence when the solar zenith angle is large (as in the Persian Gulf case). However, limb brightening does have some spectral dependence, being more pronounced for shorter wavelengths (0.472-0.675 μm), where Rayleigh and aerosol scattering is more prevalent.

Calculated surface-atmosphere system albedos for ocean water are presented in Table 2e and Plate 5a. For this ocean surface, the measured nadir-reflectance is 37% more than the hemispherical albedo for the 0.472 μm channel, but nadir-reflectances exceed the calculated hemispherical albedos by 100-160% for all other channels for this surface-atmosphere system.

One week earlier, on July 20, the C-131A measured the BRF of the Atlantic Ocean in roughly the same area it did on July 27 when the sun was considerably lower in the sky (solar zenith angle was 59° instead of 19°). The AATS-6 recorded an aerosol layer above the aircraft (altitude: 0.27 km) with an Ångström exponent of 1.3 ± 0.1 and an optical thickness of 0.055 ± 0.003 at 0.451 μm [Russell *et al.*, 1999]. The four orbits took only 8 minutes, during which time the solar zenith angle varied by only 1.5° . The ocean BRF measured on this day is qualitatively very similar to the Persian Gulf BRF presented previously. In this case, the measured nadir-reflectance is 78% less than the hemispherical albedo for the 0.472 μm channel, but nadir-reflectances are less than the calculated hemispherical albedos by about 95% for this surface-atmosphere system (see Table 2f).

5. SUMMARY

To effectively monitor the Earth's climate, it will be necessary to accurately interpret satellite measurements of top-of-the-atmosphere radiance, so that parameters that influence the Earth's radiation budget can be well estimated. Because radiances obtained from satellite measurements are influenced by the sur-

face-atmosphere system as a whole, it is necessary to know the bidirectional reflectance functions for various surfaces, so that radiative effects of natural surfaces may be taken into consideration for remote sensing of aerosols and clouds, and also so that accurate surface hemispherical albedos can be input into GCMs.

During SCAR-A, the Kuwait Oil Fire Smoke Experiment, and TARFOX, surface spectral bidirectional reflectances were measured of haze over forested wetland (July 28, 1993), desert (May 28, 1991), gulf water (May 28, 1991), and ocean water (July 27, 1996) using the Cloud Absorption Radiometer (CAR) under cloud-free conditions. Although the CAR measurements are contaminated by Rayleigh and aerosol scattering and minor gaseous absorption, results show distinct spectral characteristics for all types of surfaces presented here. These detailed measurements of the angular distribution of spectral reflectance have been used to compute hemispherical albedos for each surface-atmosphere system. Large differences were found between these spectral-hemispherical albedos and their corresponding measured nadir reflectances, up to 160%.

The CAR measurements, combined with the boundary layer aircraft measurements of aerosol physical properties and other co-located observations, form an unprecedented data set that is expected to greatly facilitate developing more realistic radiative transfer models in the future. All BRF data were processed to level-1b (calibrated and geolocated radiances). Information on where and how to obtain CAR data from several field experiments, as well as browse images, a CAR data user's guide, and software for unpacking and interpreting CAR data, may be found on the World Wide Web at <http://ltpwww.gsfc.nasa.gov/CAR>.

Acknowledgments. The authors are especially grateful to Prof. P. V. Hobbs and all of the University of Washington personnel who helped to make these complex field projects and data collection a success. This research was supported by

funding provided by National Science Foundation grant ATM-9114993, National Geographic Society grant 10727-91, the NASA Radiation Processes Science Program, the MODIS Science Team, and the EOS Project Science Office.

REFERENCES

- Ahmad, S. P., and D. W. Deering, A simple analytical function for bidirectional reflectance, *J. Geophys. Res.*, *97*, 18867-18886, 1999.
- Arnold, G. T., S. C. Tsay, M. D. King, and J. Y. Li, Airborne spectral measurements of surface anisotropy of Arctic sea ice and tundra during LEADDEX and ARMCAS, submitted to *Int. J. Remote Sens.*, 1999.
- Barnsley, M. J., A. H. Strahler, K. P. Morris, and J. P. Muller, Sampling the surface bidirectional reflectance distribution function (BRDF): 1. Evaluation of current and future satellite sensors, *Remote Sens. Rev.*, *8*, 271-311, 1994.
- Berk, A., L. Bernstein, and D. Robertson, MODTRAN: A moderate resolution model for LOWTRAN 7, final report, *Geophysics Laboratory, GL-TR-89-0122*, April, 1989.
- Bréon, F. M., V. Vanderbilt, M. Leroy, P. Bicheron, C. L. Walthall, and J. E. Kalshoven, Evidence of hot spot directional signature from airborne POLDER measurements, *IEEE Trans. Geosci. Remote Sens.*, *35*, 479-484, 1994.
- Curry, J. A., P. V. Hobbs, M. D. King, D. A. Randall, P. Minnis, G. A. Isaac, J. O. Pinto, T. Uttal, A. Bucholtz, D. G. Cripe, H. Gerber, C. W. Fairall, T. J. Garrett, J. Hudson, J. M. Intrieri, C. Jakob, T. Jensen, P. Lawson, D. Marcotte, L. Nguyen, P. Pilewskie, A. Rangno, D. Rodgers, K. B. Strawbridge, F. P. J. Valero, A. G. Williams, and D. Wylie, FIRE Arctic Clouds Experiment, *Bull. Amer. Meteor. Soc.*, in press, 1999.
- Chandrasekhar, S., *Radiative Transfer*, 393 pp., Dover, New York, 1960.
- Deering, D. W., T. F. Eck, and J. Otterman, Bidirectional reflectances of selected desert surfaces and their three-parameter soil characterization, *Agric. Forest Meteor.*, *52*, 71-93, 1990.
- Deering, D. W., T. F. Eck, and B. Banerjee, Characterization of the reflectance ani-

- sotropy of three boreal forest canopies in spring-summer, *Remote Sens. Environ.*, *67*, 205-229, 1999.
- Hapke, B., *Theory of Reflectance and Emittance Spectroscopy*, 455 pp., Cambridge University Press, 1993.
- Hapke, B., D. DiMucci, R. Nelson, and W. Smythe, The cause of the hot spot in vegetation canopies and soils: Shadow-hiding versus coherent backscatter, *Remote Sens. Environ.*, *58*, 63-68, 1996.
- Holben, B. N., T. F. Eck, I. Slutsker, D. Tanré, J. P. Buis, A. Setzer, E. Vermote, J. A. Reagan, Y. J. Kaufman, T. Nakajima, F. Lavenue, I. Jankowiak, and A. Smirnov, AERONET—A federated instrument network and data archive for aerosol characterization, *Remote Sens. Environ.*, *66*, 1-16, 1998.
- Hobbs, P. V., and L. F. Radke, Airborne studies of the smoke from the Kuwait oil fires, *Science*, *256*, 987-991, 1992.
- Jupp, D. L. B., and A. H. Strahler, A hotspot model for leaf canopies, *Remote Sens. Environ.*, *38*, 193-210, 1991.
- Kimes, D. S., P. J. Sellers, and D. J. Diner, Extraction of spectral hemispherical reflectance (albedo) of surface from nadir and directional reflectance data, *Int. J. Remote Sens.*, *8*, 1727-1746, 1987.
- King, M. D., M. G. Strange, P. Leone and L. R. Blaine, Multiwavelength scanning radiometer for airborne measurements of scattered radiation within clouds, *J. Atmos. Oceanic Technol.*, *3*, 513-522, 1986.
- King, M. D., Directional and spectral reflectance of the Kuwait Oil-Fire smoke, *J. Geophys. Res.*, *97*, 14545-14549, 1992.
- King, M. D., W. P. Menzel, P. S. Grant, J. S. Myers, G. T. Arnold, S. E. Platnick, L. E. Gumley, S. C. Tsay, C. C. Moeller, M. Fitzgerald, K. S. Brown, and F. G. Osterwisch, Airborne scanning spectrometer for remote sensing of cloud,

- aerosol, water vapor, and surface properties, *J. Atmos. Oceanic. Technol.*, *13*, 777-794, 1996.
- King, M. D., and R. Greenstone (Eds.), 1999 EOS Reference Handbook, *Rep. NASA NP-1999-08-134-GSFC*, 361 pp., NASA Goddard Space Flight Center, Greenbelt, MD., 1999.
- Pilewskie, P., and F. P. J. Valero, Radiative effects of the smoke clouds from the Kuwait oil fires, *J. Geophys. Res.*, *97*, 14541-14544, 1992.
- Ross, J. K., and A. L. Marshak, The influence of leaf orientation and the specular component of leaf reflectance on the canopy bidirectional reflectance, *Remote Sens. Environ.*, *27*, 251-260, 1989.
- Russell, P. B., J. M. Livingston, P. Hignett, S. Kinne, J. Wong, A. Chien, R. Bergstrom, P. Durkee, and P. V. Hobbs, Aerosol-induced radiative flux changes off the United States mid-Atlantic coast: Comparison of values calculated from sunphotometer and in situ data with those measured by airborne pyranometer, *J. Geophys. Res.*, *104*, 2289-2307, 1999.
- SCAR-A (Sulphates, Clouds, and Radiation – Atlantic) Mission Summary Report*, April 1994, available from SCAR Project Office, MS 483, NASA Langley Research Center, Hampton, VA 23681-0001.
- Strahler, A. H., and D. L. B. Jupp, Modeling bidirectional reflectance of forest and woodlands using Boolean models and geometric optics, *Remote Sens. Environ.*, *34*, 153-166, 1990.
- Tsay, S. C., M. D. King, G. T. Arnold, and J. Y. Li, Airborne spectral measurements of surface anisotropy during SCAR-B, *J. Geophys. Res.*, *103*, 31943-31953, 1998.
- van de Hulst, H. C., *Multiple Light Scattering: Tables, Formulas, and Applications*. 739 pp., Academic Press, 1980.

Table 1. Cloud Absorption Radiometer specifications during field campaigns.

Platform	University of Washington C-131A aircraft
Ground speed	80 m s ⁻¹ (nominal)
Total field of view	190°
Instantaneous field of view	17.5 mrad (1°)
Pixels per scan line	395
Scan rate	100 scan lines per minute
Spectral channels	13 (7 continuously sampled and 6 in filter wheel)
Spectral range	0.472 (0.507) - 2.303 μm
Data system	8 channels @ 10 bits
Calibration	Integrating sphere on the ground

Table 2. Computed spectral albedo (surface-atmosphere system) and measured nadir reflectance for (a, b) the Great Dismal Swamp with overlying haze layer, (c) Saudi Arabian Desert, (d) Persian Gulf water, and (e, f) Atlantic Ocean water. Uncertainties do not include possible errors in calibration.

Central wave- length (μm)	Bandwidth (μm)	Solar flux ($\text{Wm}^{-2}\mu\text{m}^{-1}$)	Solar zenith angle	Albedo	Nadir reflectance
(a) Great Dismal Swamp with Haze Layer: July 28, 1993 (9:13 – 9:22 local time)					
0.472	0.021	1959.0	53.17° - 54.84°	0.054 ± 0.001	0.020 ± 0.003
0.675	0.020	1469.0	53.17° - 54.84°	0.038 ± 0.001	0.015 ± 0.005
0.754	0.009	1205.2	53.17° - 54.84°	0.27 ± 0.01	0.23 ± 0.04
0.869	0.020	940.48	53.17° - 54.84°	0.34 ± 0.02	0.29 ± 0.06
1.038	0.020	669.71	53.17° - 54.84°	0.36 ± 0.02	0.31 ± 0.05
1.219	0.020	474.08	53.17° - 54.84°	0.253 ± 0.008	0.22 ± 0.04
1.271	0.021	429.24	53.17° - 54.84°	0.282 ± 0.010	0.24 ± 0.04
1.643	0.041	229.15	54.00° - 54.84°	0.157 ± 0.005	0.13 ± 0.03
2.207	0.040	72.117	53.17° - 53.57°	0.061	0.05 ± 0.02
(b) Great Dismal Swamp with Haze Layer: July 28, 1993 (12:11 – 12:20 local time)					
0.472	0.021	1959.0	20.98° - 22.14°	0.0271 ± 0.0002	0.016 ± 0.002
0.675	0.020	1469.0	20.98° - 22.14°	0.0153 ± 0.0004	0.011 ± 0.004
0.754	0.009	1205.2	20.98° - 22.14°	0.239 ± 0.002	0.26 ± 0.03
0.869	0.020	940.48	20.98° - 22.14°	0.304 ± 0.003	0.33 ± 0.04
1.038	0.020	669.71	20.98° - 22.14°	0.320 ± 0.003	0.35 ± 0.04
1.219	0.020	474.08	20.98° - 22.14°	0.240 ± 0.003	0.26 ± 0.03
1.271	0.021	429.24	20.98° - 22.14°	0.268 ± 0.003	0.29 ± 0.03
1.643	0.041	229.15	21.57° - 22.14°	0.137 ± 0.002	0.16 ± 0.02

2.207	0.040	72.117	20.98° - 21.27°	0.052	0.06 ± 0.01
-------	-------	--------	-----------------	-------	-------------

(c) Saudi Arabian Desert: May 28, 1991 (16:28 - 16:30 local time)

0.503	0.021	1854.4	48.05° - 48.53°	0.212	0.16 ± 0.02
0.673	0.020	1485.6	48.05° - 48.53°	0.322	0.28 ± 0.03
0.754	0.009	1249.3	48.05° - 48.53°	0.342	0.31 ± 0.03
0.866	0.020	924.29	48.05° - 48.53°	0.385	0.34 ± 0.04
1.031	0.020	689.19	48.05° - 48.53°	0.383	0.35 ± 0.04
1.220	0.020	485.29	48.05° - 48.53°	0.357	0.33 ± 0.03
1.270	0.021	400.31	48.05° - 48.53°	0.365	0.34 ± 0.03

(d) Persian Gulf water: May 28, 1991 (17:03-17:07 local time)

0.503	0.021	1854.4	55.83° - 56.86°	0.101 ± 0.006	0.044 ± 0.009
0.673	0.020	1485.6	55.83° - 56.86°	0.096 ± 0.007	0.033 ± 0.004
0.754	0.009	1249.3	55.83° - 56.86°	0.099 ± 0.008	0.030 ± 0.004
0.866	0.020	924.29	55.83° - 56.86°	0.097 ± 0.007	0.027 ± 0.004
1.031	0.020	689.19	55.83° - 56.86°	0.087 ± 0.007	0.026 ± 0.004
1.220	0.020	485.29	55.83° - 56.86°	(saturated)	0.022 ± 0.004
1.270	0.021	400.31	55.83° - 56.86°	0.081 ± 0.007	0.021 ± 0.003

(e) Atlantic Ocean: July 27, 1996 (12:34 - 12:43 local time)

0.472	0.021	1989.8	19.10° - 19.53°	0.0492 ± 0.0004	0.07 ± 0.02
0.675	0.020	1491.9	19.10° - 19.53°	0.0284 ± 0.0008	0.06 ± 0.02
0.869	0.020	956.55	19.10° - 19.53°	0.0270 ± 0.0003	0.06 ± 0.03
1.038	0.020	680.34	19.10° - 19.53°	0.0242 ± 0.0003	0.06 ± 0.02
1.219	0.020	481.59	19.10° - 19.53°	0.0204 ± 0.0002	0.05 ± 0.02
1.271	0.021	436.72	19.10° - 19.53°	0.0212 ± 0.0002	0.05 ± 0.02

1.643	0.041	232.79	19.29° - 19.53°	0.0217 ± 0.0004	0.06 ± 0.02
2.207	0.040	73.240	19.10° - 19.19°	0.0229 ± 0.0005	0.06 ± 0.03

(f) Atlantic Ocean: July 20, 1996 (17:22 – 17:30 local time)

0.472	0.021	1956.5	58.17° - 59.73°	0.058 ± 0.004	0.013 ± 0.002
0.675	0.020	1467.2	58.17° - 59.73°	0.056 ± 0.006	0.003 ± 0.004
0.869	0.020	939.32	58.17° - 59.73°	0.059 ± 0.006	0.002 ± 0.002
1.038	0.020	668.88	58.17° - 59.73°	0.042 ± 0.005	0.002 ± 0.004
1.219	0.020	473.49	58.17° - 59.73°	0.038 ± 0.004	0.002 ± 0.002
1.271	0.021	429.21	58.17° - 59.73°	0.061 ± 0.007	0.002 ± 0.002

FIGURE LEGEND

Figure 1. Schematic illustration of a clockwise circular flight track for measuring surface bidirectional reflectance. The roll angle of the plane is r .

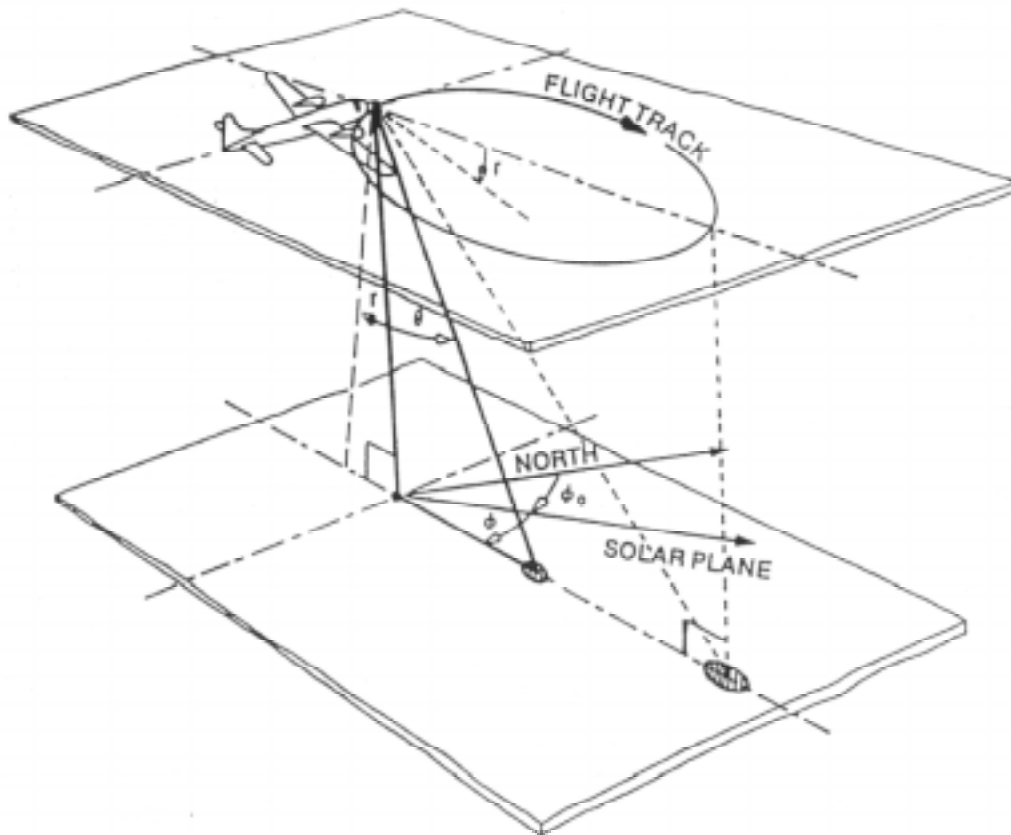


Figure 1. Schematic illustration of a clockwise circular flight track for measuring surface bidirectional reflectance. The roll angle of the plane is r .

PLATE LEGENDS

- Plate 1. Images of (a) Saudi Arabian Desert and (b) the Great Dismal Swamp south of Norfolk, Virginia. The image of the Saudi Arabian Desert was acquired by the Landsat thematic mapper on June 12, 1990, one year before the 1991 Kuwaiti oil fires. The RGB assignment is red ($2.2 \mu\text{m}$), green ($0.66 \mu\text{m}$), and blue ($0.49 \mu\text{m}$). The insert shows the location of the BRF-measurement site. The photograph of the Great Dismal Swamp was taken during SCAR-A from the University of Washington C-131A aircraft.
- Plate 2. Composite image of the Great Dismal Swamp south of Norfolk, Virginia, taken using the MODIS Airborne Simulator from the NASA ER-2 aircraft on July 28, 1993. The RGB assignment is red ($2.14 \mu\text{m}$), green ($0.94 \mu\text{m}$), and blue ($0.66 \mu\text{m}$). This image was resampled to a constant resolution of 60 m. The solar zenith angle was $\theta_0 = 31^\circ$ and the aircraft was flying from top to bottom down the center of this image, such that the MAS scan was near the principal plane of the sun. The hotspot in the antisolar direction ($\theta = 31^\circ$, $\phi = 180^\circ$) is clearly evident as a yellow band down the left hand portion of the image. Sun glint in the specular direction ($\theta = 31^\circ$, $\phi = 0^\circ$) is evident over surface water on the right-hand portion of the image.
- Plate 3. Spectral measurements of the surface-atmosphere system bidirectional reflectance over the Great Dismal Swamp on July 28, 1993 during SCAR-A. The location of the anti-solar point at $\theta = 54^\circ$ and $\phi = 180^\circ$ is indicated in Plate 3a.

- Plate 4. Angular distribution of BRF in the principal plane for (a) the Great Dismal Swamp with overlying haze using MAS data presented in Plate 2, (b) the Great Dismal Swamp with overlying haze using CAR data presented in Plate 3, and (c) Saudi Arabian Desert during KOFSE.
- Plate 5. Hemispherical albedo, nadir reflectance, and ratio of nadir reflectance to hemispherical albedo plotted as a function of wavelength for each surface-atmosphere system. The ratio of nadir reflectance to hemispherical albedo is not affected by errors in calibration.
- Plate 6. Spectral measurements of the surface-atmosphere system bidirectional reflectance over Saudi Arabia on May 28, 1991 during KOFSE. The location of the anti-solar point at $\theta = 48^\circ$ and $\phi = 180^\circ$ is indicated in Plate 6a.
- Plate 7. Spectral measurements of the surface-atmosphere system bidirectional reflectance over the Persian Gulf on May 28, 1991 during KOFSE. The location of the anti-solar point at $\theta = 56^\circ$ and $\phi = 180^\circ$ is indicated in Plate 7a.
- Plate 8. Angular distribution of BRF in the principal plane for (a) Persian Gulf water during KOFSE, and (b) the Atlantic Ocean during TARFOX.
- Plate 9. Spectral measurements of the surface-atmosphere system bidirectional reflectance above the Atlantic Ocean on July 27, 1996 during TARFOX. The location of the anti-solar point at $\theta = 20^\circ$ and $\phi = 180^\circ$ is indicated in Plate 9a.

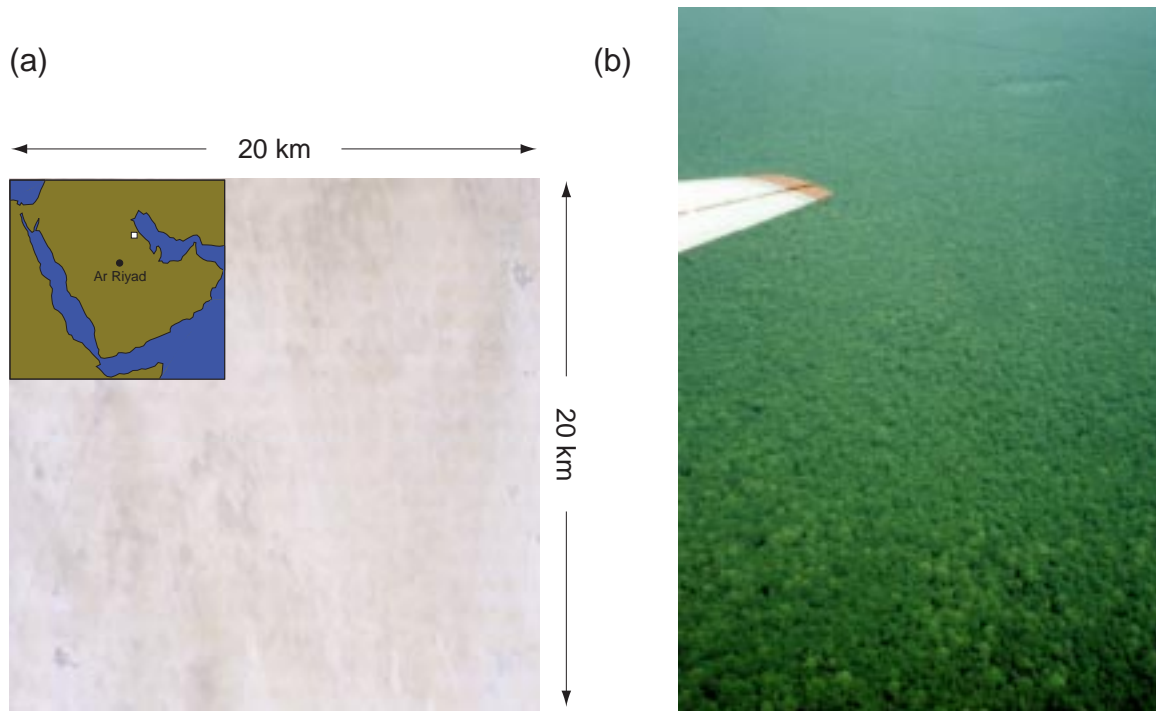


Plate 1. Images of (a) Saudi Arabian Desert and (b) the Great Dismal Swamp south of Norfolk, Virginia. The image of the Saudi Arabian Desert was acquired by the Landsat thematic mapper on June 12, 1990, one year before the 1991 Kuwait oil fires. The RGB assignment is red ($2.2 \mu\text{m}$), green ($0.66 \mu\text{m}$), and blue ($0.49 \mu\text{m}$). The insert shows the location of the BRF-measurement site. The photograph of the Great Dismal Swamp was taken during SCAR-A from the University of Washington C-131A aircraft.

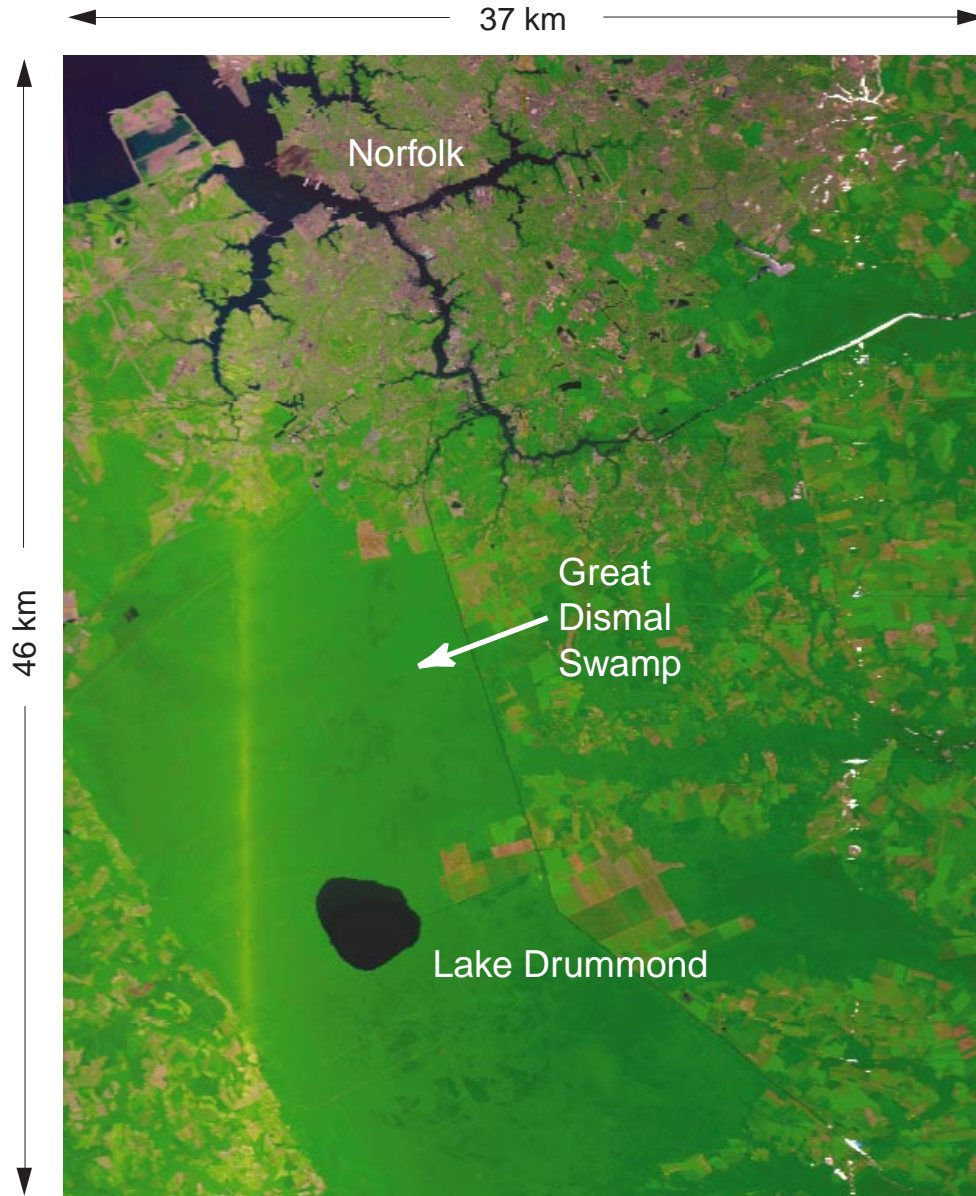


Plate 2. Composite image of the Great Dismal Swamp south of Norfolk, Virginia, taken using the MODIS Airborne Simulator from the NASA ER-2 aircraft on July 28, 1993. The RGB assignment is red ($2.14 \mu\text{m}$), green ($0.94 \mu\text{m}$), and blue ($0.66 \mu\text{m}$). This image was resampled to a constant resolution of 60 m. The solar zenith angle was $\theta_0 = 31^\circ$ and the aircraft was flying from top to bottom down the center of this image....

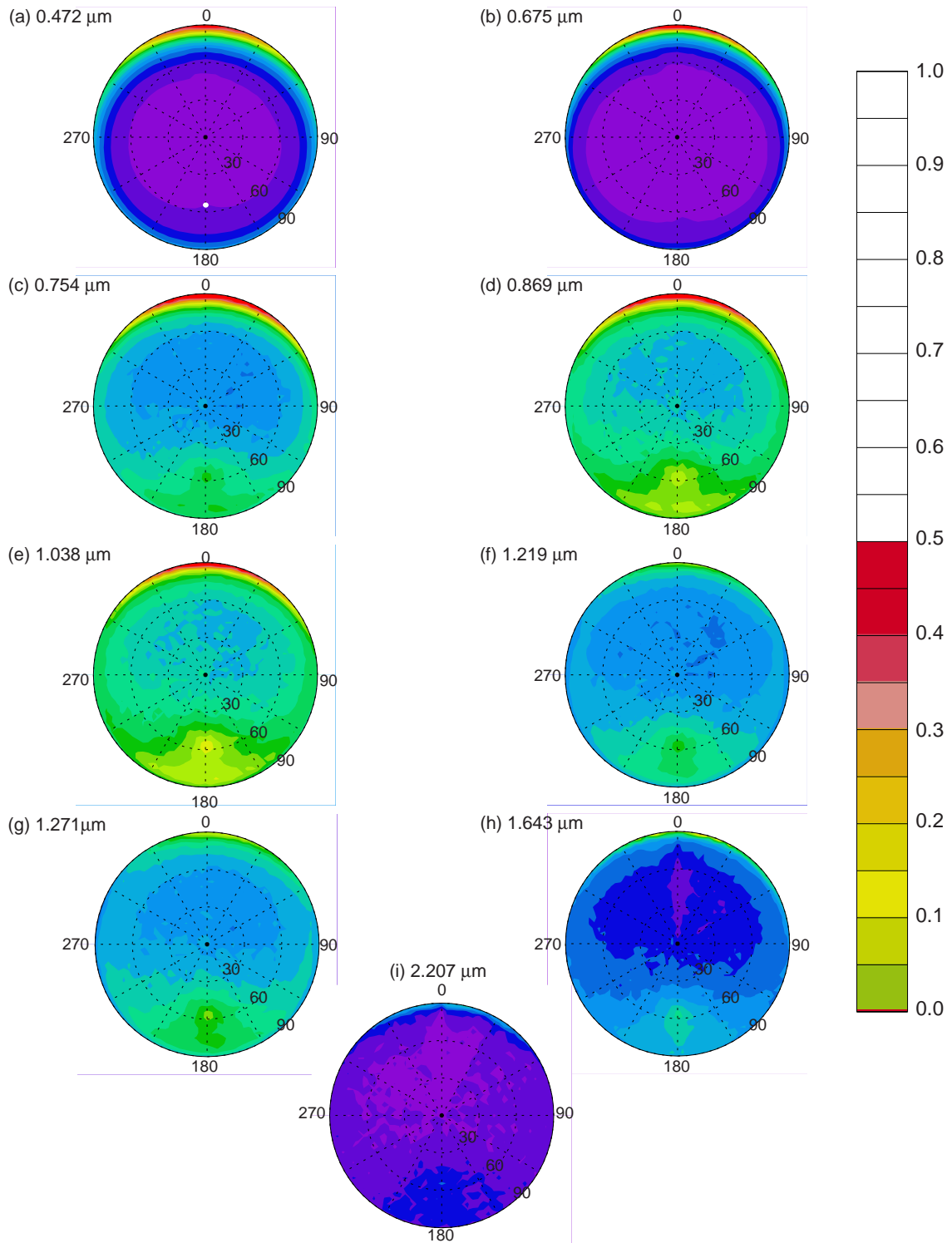


Plate 3. Spectral measurements of the surface-atmosphere system bidirectional reflectance over the Great Dismal Swamp on July 28, 1993 during SCAR-A. The location of the anti-solar point at $\theta = 54^\circ$ and $\phi = 180^\circ$ is indicated in Plate 3a.

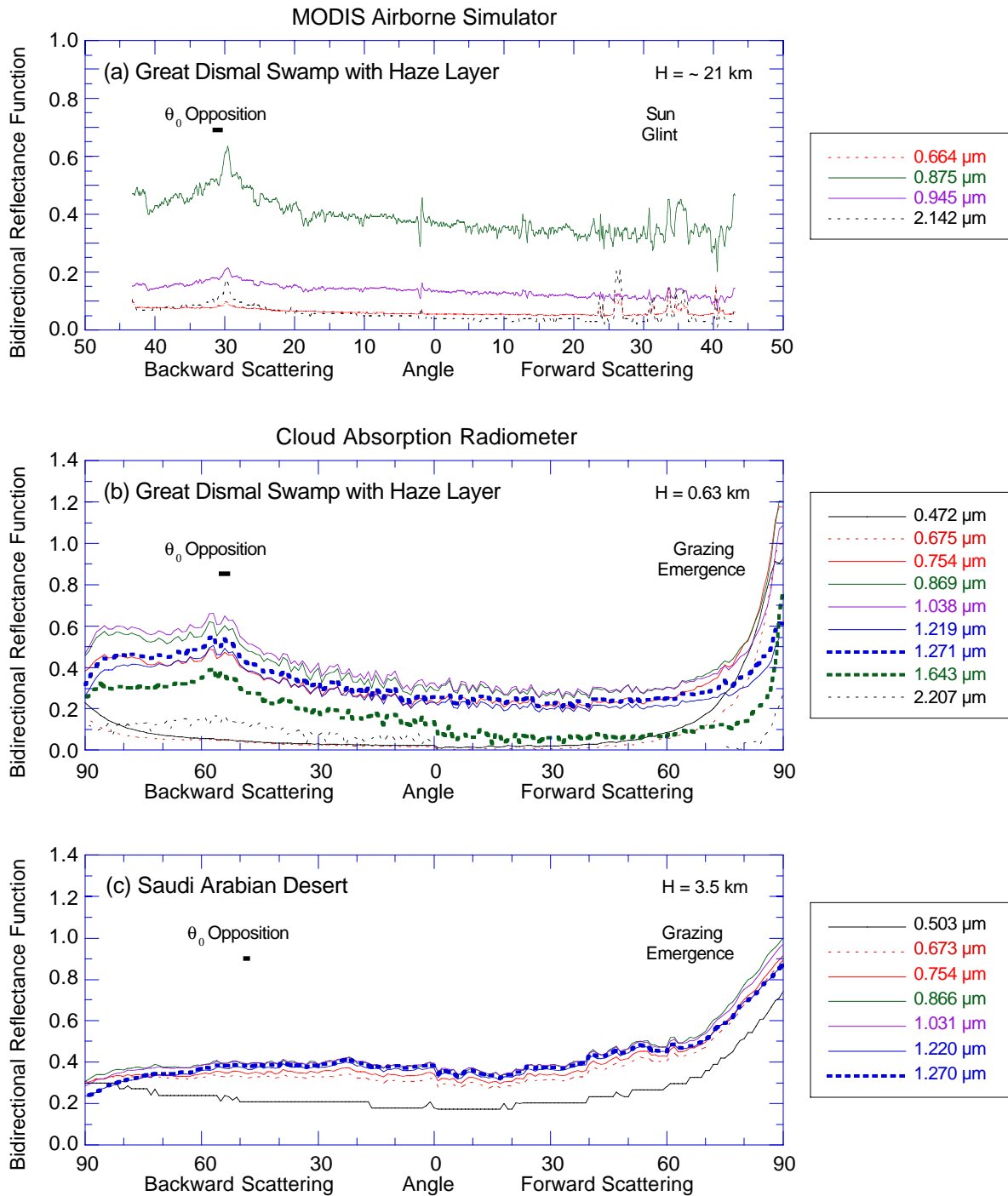


Plate 4. Angular distribution of BRF in the principal plane for (a) the Great Dismal Swamp with overlying haze using MAS data presented in Plate 2, (b) the Great Dismal Swamp with overlying haze using CAR data presented in Plate 3, and (c) Saudi Arabian Desert during KOFSE.

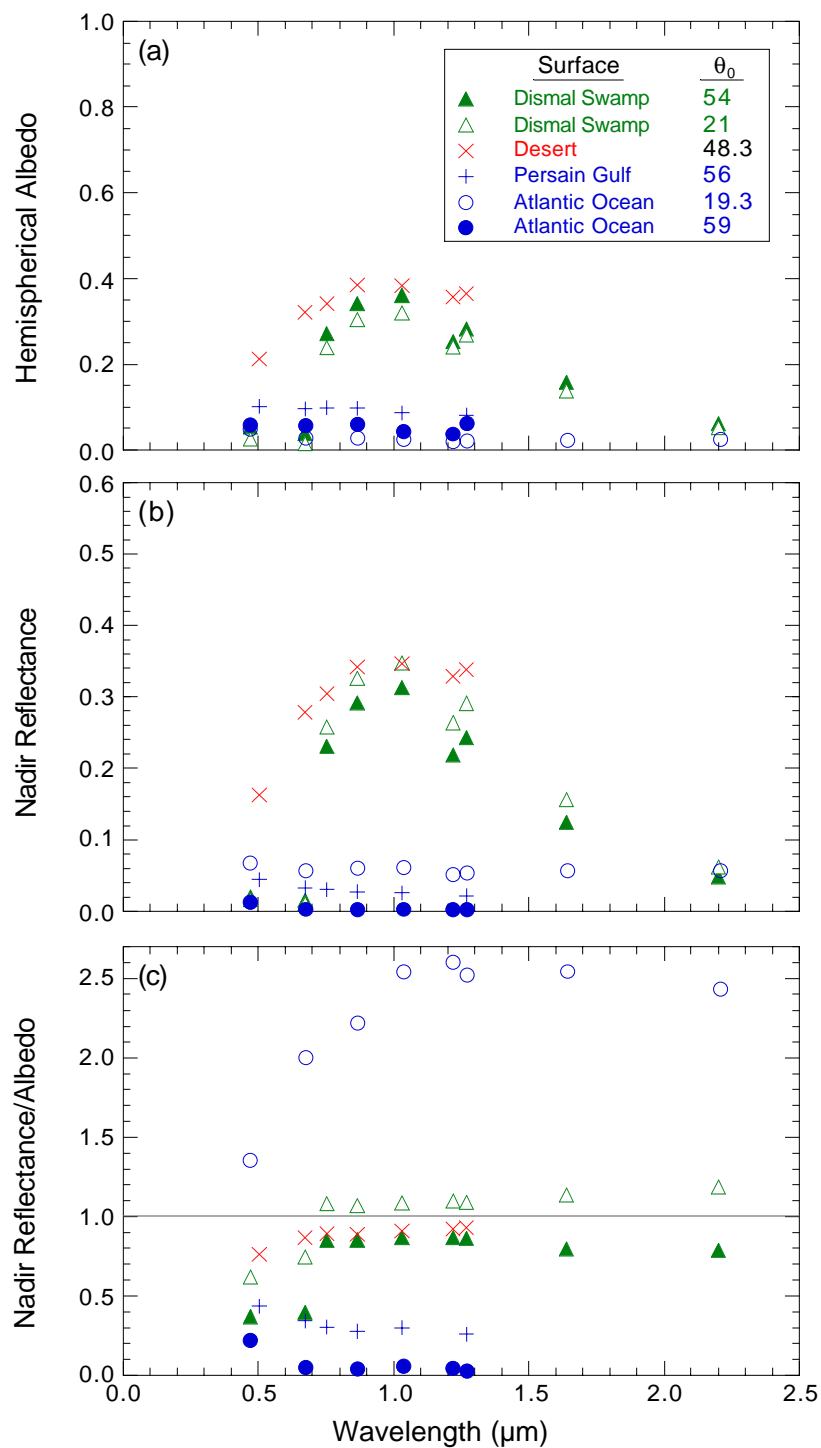


Plate 5. Hemispherical albedo, nadir reflectance, and ratio of nadir reflectance to hemispherical albedo plotted as a function of wavelength for each surface-atmosphere system. The ratio of nadir reflectance to hemispherical albedo is not affected by errors in calibration.

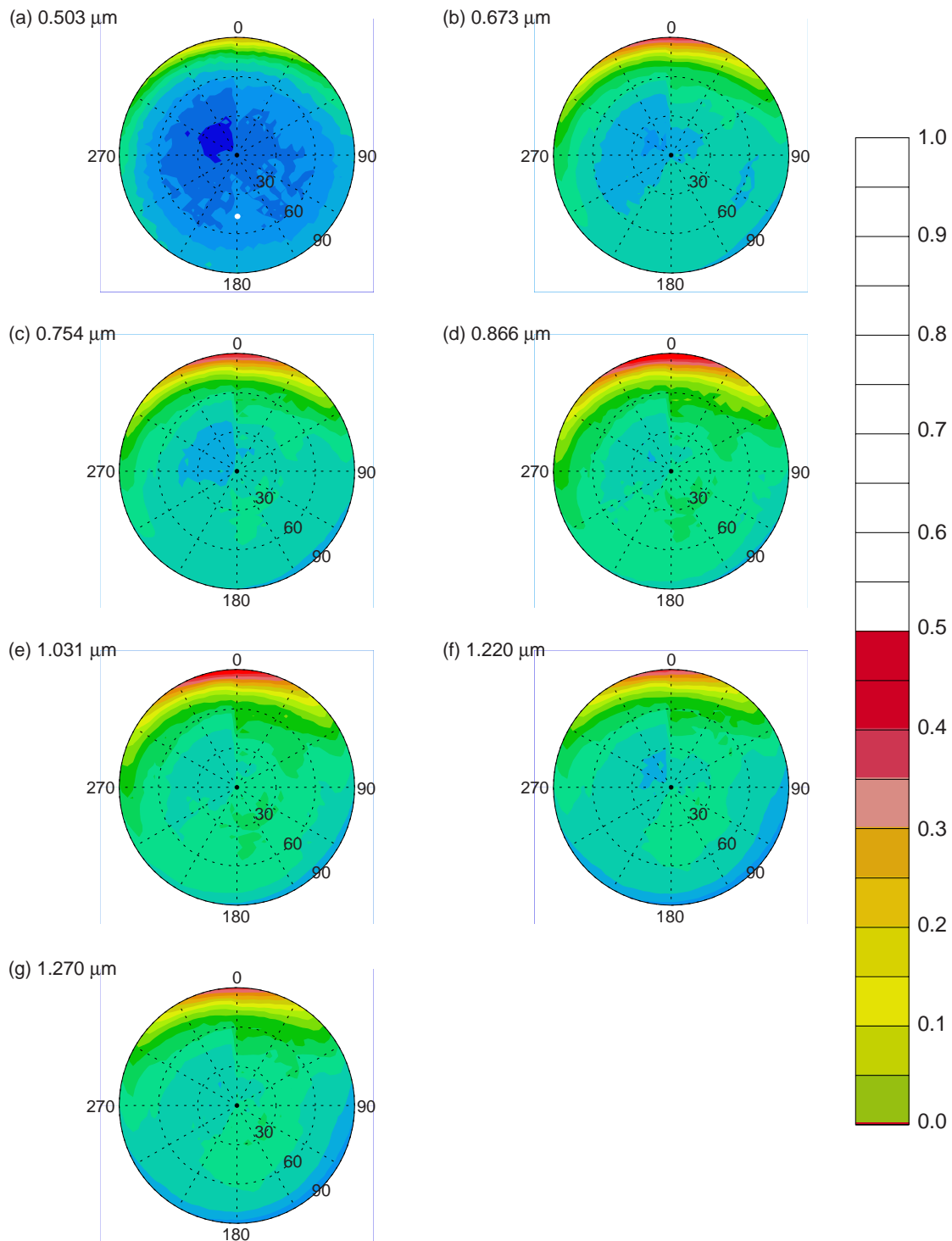


Plate 6. Spectral measurements of the surface-atmosphere system bidirectional reflectance over Saudi Arabia on May 28, 1991 during KOFSE. The location of the anti-solar point at $\theta = 48^\circ$ and $\phi = 180^\circ$ is indicated in Plate 6a.

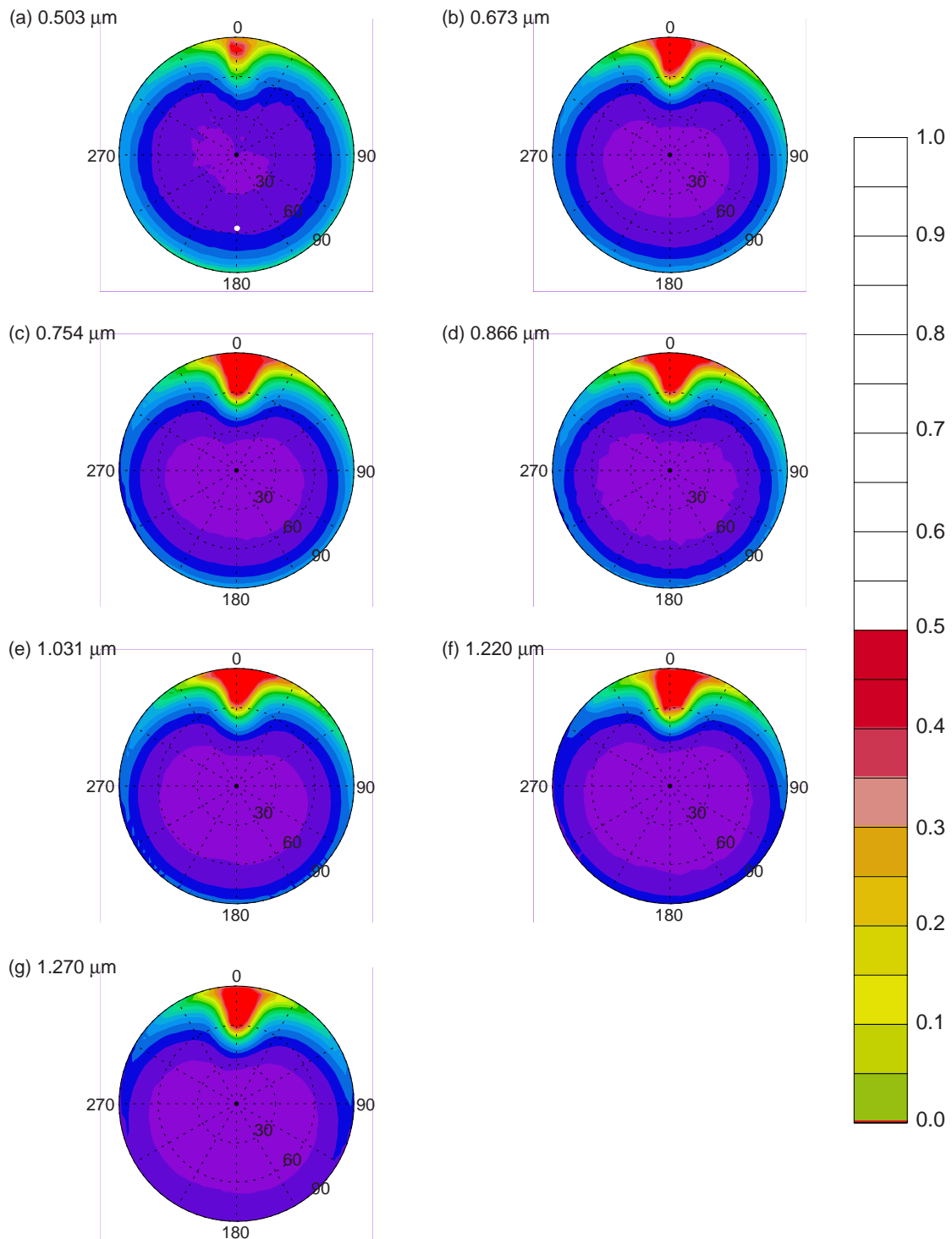


Plate 7. Spectral measurements of the surface-atmosphere system bidirectional reflectance over the Persian Gulf on May 28, 1991 during KOFSE. The location of the anti-solar point at $\theta = 56^\circ$ and $\phi = 180^\circ$ is indicated in Plate 7a.

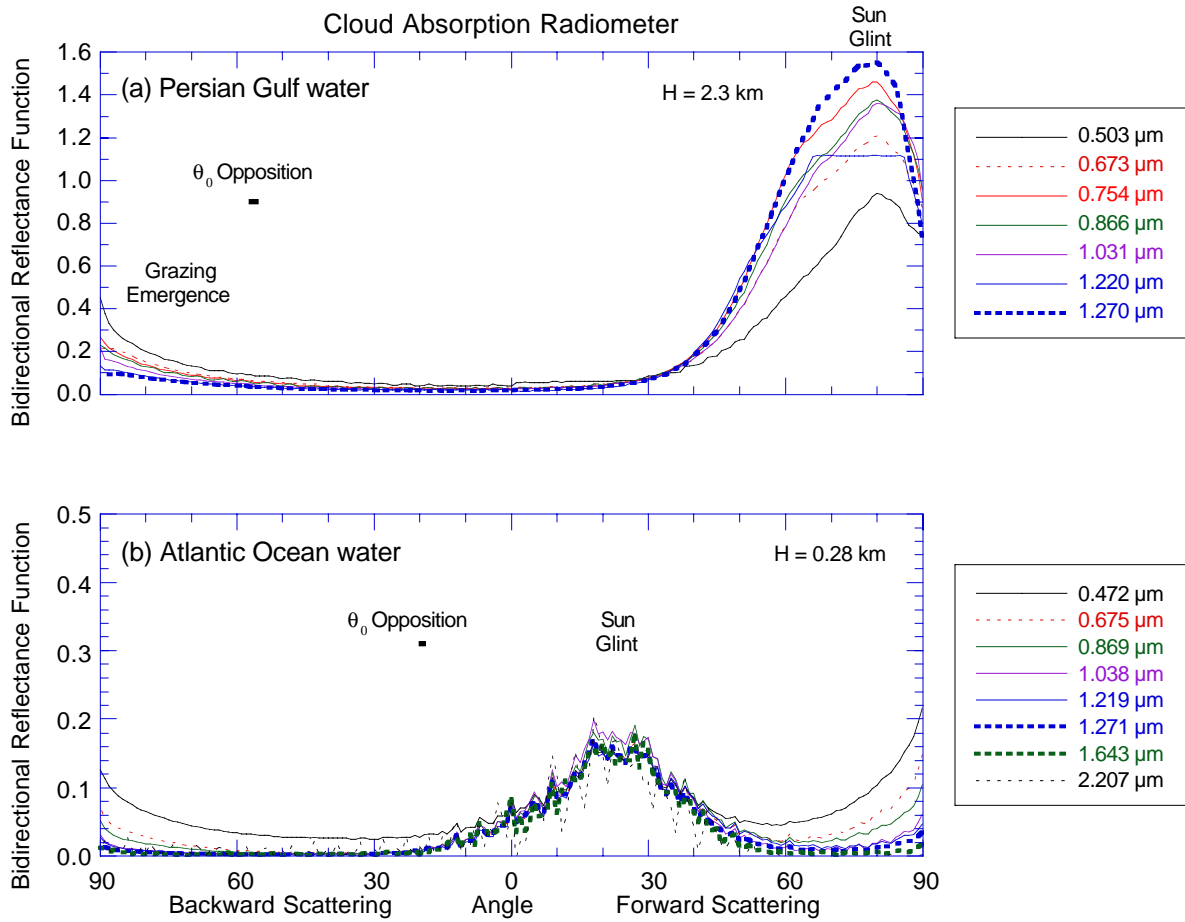


Plate 8. Angular distribution of BRF in the principal plane for (a) Persian Gulf water during KOFSE, and (b) the Atlantic Ocean during TARFOX.

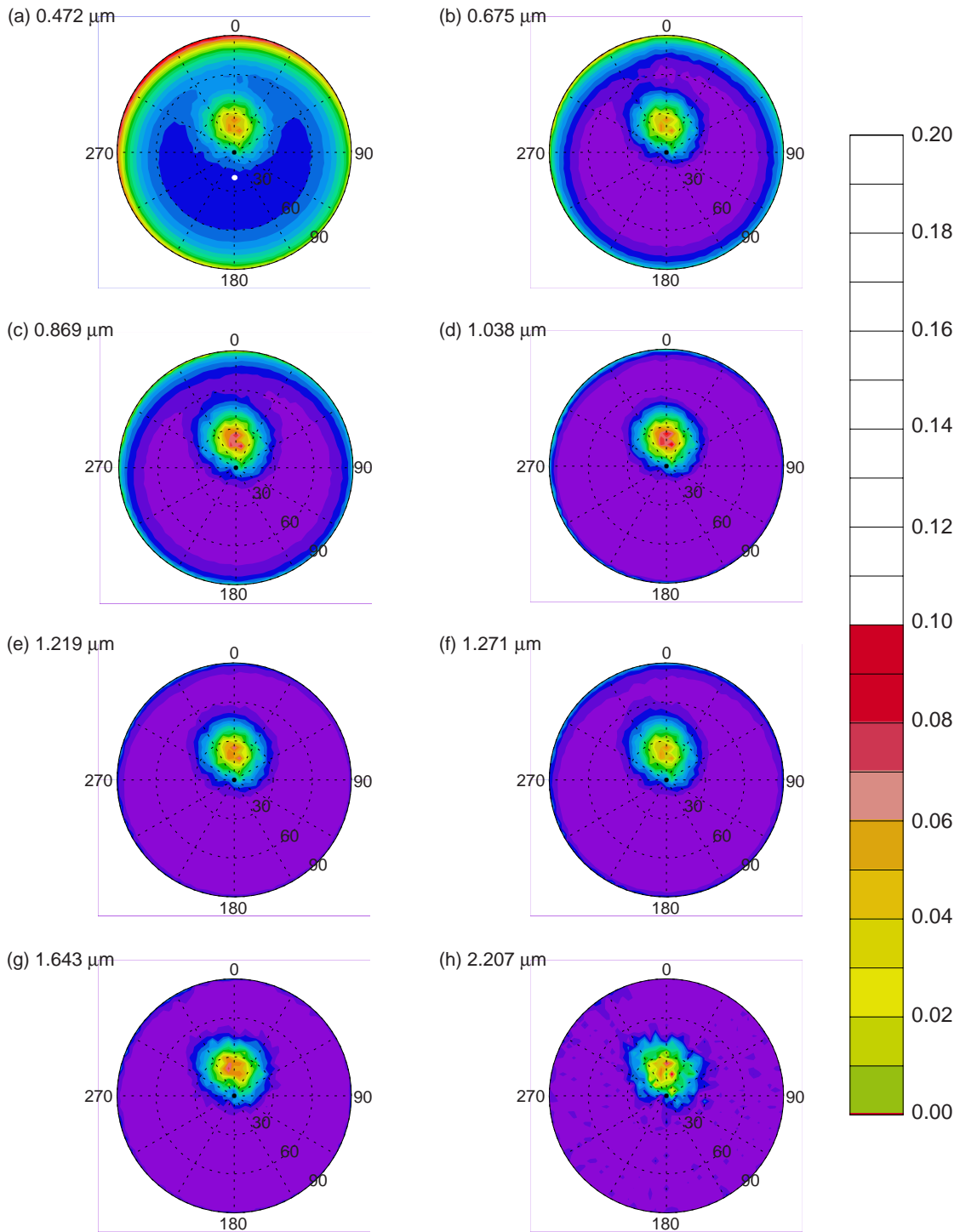


Plate 9. Spectral measurements of the surface-atmosphere system bidirectional reflectance above the Atlantic Ocean on July 27, 1996 during TARFOX. The location of the anti-solar point at $\theta = 20^\circ$ and $\phi = 180^\circ$ is indicated in Plate 9a.